

# 2 **Measuring directionality in double-beta decay and** 3 **neutrino interactions with kiloton-scale scintillation** 4 **detectors**

---

**C. Aberle<sup>a</sup>, A. Elagin<sup>b</sup>, H.J. Frisch<sup>b</sup>, M. Wetstein<sup>b</sup>, and L. Winslow<sup>a\*</sup>**

<sup>a</sup>*University of California, Los Angeles, Los Angeles, CA 90095, USA*

<sup>b</sup>*University of Chicago, Chicago, IL 60637, USA*

5 *E-mail: lwinslow@physics.ucla.edu*

ABSTRACT: Large liquid-scintillator-based detectors have proven to be exceptionally effective for low energy neutrino measurements due to their good energy resolution and scalability to large volumes. The addition of directional information using Cherenkov light and fast timing would enhance the scientific reach of these detectors, especially for searches for neutrino-less double-beta  
6 decay. In this paper, we develop a technique for extracting particle direction using the difference in arrival times for Cherenkov and scintillation light, and evaluate several detector advances in timing, photodetector spectral response, and scintillator emission spectra that could be used to make direction reconstruction a reality in a kiloton-scale detector.

7 **KEYWORDS:** Scintillators, Large detector systems for particle and astroparticle physics; Neutrino  
8 detectors; Simulation methods and programs.

---

\*corresponding author

---

## Contents

11	<b>1. Introduction</b>	<b>1</b>
12	<b>2. Liquid scintillator detectors</b>	<b>2</b>
13	<b>3. Geant4 simulation</b>	<b>5</b>
14	<b>4. Detector timing</b>	<b>8</b>
15	<b>5. Detector wavelength response</b>	<b>9</b>
16	<b>6. Scintillator emission spectrum</b>	<b>9</b>
17	<b>7. Reconstruction</b>	<b>10</b>
18	<b>8. Energy dependence</b>	<b>12</b>
19	<b>9. Conclusions</b>	<b>13</b>

---

## 1. Introduction

Liquid scintillator-based detectors are responsible for several of the critical measurements that have determined our present understanding of neutrino masses and mixings. These measurements include KamLAND's measurement of reactor anti-neutrino oscillation at a distance of  $\sim 200$  km[1], Borexino's measurement of  $^7\text{Be}$  solar neutrino oscillation[2], and most recently the short baseline reactor anti-neutrino experiments that measured oscillations due to  $\theta_{13}$  at a distance of 1 km: Daya Bay[3], Double Chooz[4, 5], and RENO[6]. Scintillator-based neutrino detectors will continue to be important for the next set of neutrino measurements, from the determination of the neutrino mass hierarchy[7, 8] to elastic scattering measurements[9] and sterile neutrino searches[10, 11], and for non-proliferation applications[12, 13].

The scalability of these detectors to large volumes also makes them highly competitive for neutrino-less double-beta ( $0\nu\beta\beta$ ) decay searches in which the final state consists of a pair of electrons with energies in the  $\sim 1$ -2 MeV range. The observation of this rare decay would prove that the neutrino is a Majorana particle, which would have profound consequences to our understanding of the generation of mass and may provide a possible explanation of the matter-antimatter asymmetry in the universe[14]. Currently one of the best limits for the  $0\nu\beta\beta$  half-life comes from the scintillating detector KamLAND-Zen[15].

The advantage of liquid scintillators for measurements in the  $\sim 1$  MeV range is their scalability from 1 ton to 1 kiloton while providing energy resolutions of  $\sigma(E) \sim 5\% / \sqrt{E(\text{MeV})}$ [1, 2]. This

is roughly a factor of two better than water Cherenkov detectors, the other developed technology that can be economically scaled to these large masses. However, this energy resolution is much poorer than other technologies being used for  $0\nu\beta\beta$  searches: Ge detectors[16], Te bolometers[17], tracking detectors[18], liquid Xe time projection chambers (TPCs)[19] and high pressure gaseous Xe TPCs[20].

Scintillation light is isotropic. At these low energies, it does not contain sufficient information to reconstruct the track of the outgoing particles, although at higher energies it may[21]. Cherenkov light is also produced for electrons above threshold. Most is absorbed and re-emitted as part of the scintillation processes; however some fraction retains its directional information. If this directional Cherenkov light can be isolated from the copious isotropic scintillation light, it may be possible to reconstruct the direction of the primary particle. The addition of directionality is a powerful tool for background rejection, especially for  $0\nu\beta\beta$  searches. In the high pressure TPCs, reduction factors on the order of  $10^4$  have been achieved[22]. It is also possible to look for new physics in the angular correlation of the emerging electrons[23], as has been proposed for the tracking-based detectors[18]. The addition of a directional signal would make large-scale liquid scintillator detectors more competitive for the next generation of  $0\nu\beta\beta$  searches and merits investigation.

This is the first in a series of papers exploring directionality in large-scale liquid scintillator detectors. In this paper, we develop a technique for separating the Cherenkov and scintillation light using the photon arrival times and evaluate several detector advances in timing, photodetector spectral response, and scintillator emission spectra that would allow the realization of direction reconstruction in kilo-ton scale scintillating neutrino detectors. This is different from the direction reconstruction described for high-energy neutrino interactions[21] or that for neutrons from inverse beta decay[24, 25]. We then use these results as input into a traditional direction reconstruction developed for water Cherenkov detectors. Since the reconstruction of the direction of  $\sim 1$  MeV particles has not been achieved before, we start these studies with the most simple case of a single particle at the center of the detector. We also start with an easier test case of a 5 MeV electron like that from a  $^8\text{B}$  solar neutrino interaction. With the higher photon statistics at this energy, we verify the technique and the different detector parameters that affect it. We then study the technique for two lower energies, 1.4 and 2.1 MeV, that are more relevant to  $0\nu\beta\beta$ .

## 2. Liquid scintillator detectors

Liquid scintillators are ‘cocktails’ of aromatic hydrocarbons. When charged particles move through a scintillator, the molecules are excited, predominantly via the non-localized electrons in the  $\pi$ -bonds of the phenyl groups[26]. Vibrational and rotational modes of the molecules are turned into heat within picoseconds through collisions with other molecules. Within  $\sim 10$  picoseconds, the  $\pi$ -electrons de-excite to the first excited state from higher levels through radiationless transitions. The first excited state can de-excite through photon emission. There are two characteristic times for this de-excitation, depending if the singlet state or the triplet state was excited. The singlet state will de-excite within nanoseconds while the triplet state de-excites on the order of 10’s or 100’s of nanoseconds. These two processes are fluorescence and phosphorescence respectively. The exact time constants for these processes are determined by the composition of the scintillator.

80 The absorption and emission spectra overlap at some level in all molecules. Consequently, if  
 81 there is only one type of molecule in the scintillator cocktail the light output is reduced due to inef-  
 82 ficiencies in the energy transfer through multiple absorption and re-emission processes. Aromatic  
 83 solutes or fluorophores are added to the primary solvent to shift the wavelengths of the photons  
 84 to higher values where the scintillator is more transparent. This wavelength-shifting is also used  
 85 to match the quantum efficiency as a function of wavelength for the photodetectors being used.  
 86 One typical scintillator mixture uses pseudocumene(1,2,4-trimethylbenzene) as the solvent with 1-  
 87 5 g/l of PPO (2,5-diphenyloxazole) as the fluorophore. This mixture has a peak emission at about  
 88 400 nm where bialkali photomultiplier tubes (PMTs) are most sensitive and the pseudocumene is  
 89 relatively transparent.

A good liquid scintillator will produce  $\sim 10,000$  photons isotropically per MeV of deposited energy. Although less abundant, Cherenkov light will be produced as well if a particle is moving faster than the speed of light in the medium. This light is emitted in a cone centered on the direction of the particle trajectory, and with a continuous spectrum weighted toward shorter wavelengths but extending well into the red. The spectrum is described by[27]:

$$\frac{d^2N}{d\lambda dx} = \frac{2\pi\alpha Z^2}{\lambda^2} \left[ 1 - \frac{1}{\beta^2 n(\lambda)^2} \right] \quad (2.1)$$

90 where  $N$  is the number of Cherenkov photons,  $\lambda$  is the wavelength of the photon,  $x$  is the distance  
 91 travelled by the particle,  $Z$  is the charge of the particle,  $\alpha$  is the fine structure constant,  $n(\lambda)$  is the  
 92 wavelength-dependent index of refraction and  $\beta$  is the velocity of the particle.

93 The Cherenkov light produced at wavelengths shorter than the absorption cutoff of the scintil-  
 94 lator will be absorbed and re-emitted as isotropic light, but wavelengths longer than this cutoff will  
 95 propagate across the detector, retaining their directional information. The absorption cutoff for the  
 96 example scintillator above is 370 nm. The index of refraction at  $n(370\text{nm})=1.466$  and can be trans-  
 97 lated into an effective Cherenkov threshold for electrons at 0.188 MeV. For a 5 MeV electron, this  
 98 yields 685 Cherenkov photons per event when integrating from the cutoff wavelength at 360 nm  
 99 to 550 nm, the wavelength above which a small number of photons is detected due to a standard  
 100 bialkali photocathode's quantum efficiency. Lowering the energy to 1 MeV yields 82 Cherenkov  
 101 photons between 360-550 nm.

All photons including these undisturbed Cherenkov photons will have timing determined by the group velocity[28 – 30] in the liquid,

$$v_g(\lambda) = \frac{c_{vacuum}}{n(\lambda) - dn(\lambda)/d\log(\lambda)}. \quad (2.2)$$

102 Photons at the scintillation cutoff of 370nm have a velocity of 0.191 m/ns, while photons with  
 103 wavelengths of 600 nm are appreciably faster, with a velocity of 0.203 m/ns. Since on average the  
 104 undisturbed Cherenkov photons have longer wavelengths, they will arrive before the scintillation  
 105 light, which is slowed by both the scintillation processes and the shorter wavelengths involved.  
 106 Thus, with sufficient timing resolution and sensitivity to longer wavelengths it should be possible to  
 107 separate the directional Cherenkov light and the isotropic scintillation light, and then to reconstruct  
 108 the direction of the initial particle.

109 In neutrino-electron scattering events, a single electron emerges with a distribution of energies  
 110 with a maximum energy related to the incoming neutrino's energy. In comparison,  $0\nu\beta\beta$  events

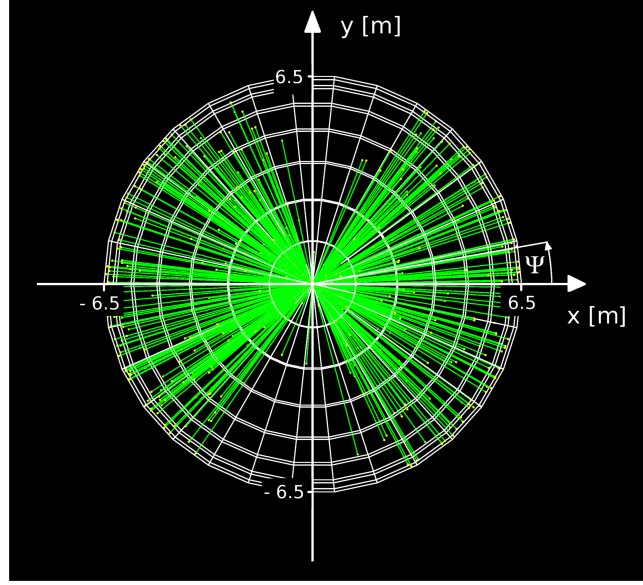


**Figure 1.** The detector geometry and coordinate system. The radial rays (green lines) are photons emitted by two back-to-back electrons with 1.4 MeV each (equally divided energy of  $^{116}\text{Cd}$   $0\nu\beta\beta$  decay). The electrons originate at the center of the sphere with initial directions along the x and -x-axis. Only Cherenkov photons are drawn to illustrate the directionality of the event.

are more complicated with two electrons emerge with a combined energy equal to the Q-value of the particular isotope. The individual electrons follow distributions of energies and angular correlations which depend on the underlying  $0\nu\beta\beta$  decay mechanism[18, 23, 31]. Figure 1 shows a simulated  $^{116}\text{Cd}$   $0\nu\beta\beta$  event in a model with light Majorana neutrino exchange, for which a probable case is the emission of two electrons with comparable energies at a large angle relative to each other.

High Q-value candidates are preferred for  $0\nu\beta\beta$  for two reasons. First, the measured half-life is inversely proportional to the phase-space factor, therefore the measured rate is expected to be higher from isotopes with higher Q-values. Second, the main background for these experiments come from the daughters of the  $^{238}\text{U}$  and  $^{232}\text{Th}$  decay chains. The Compton shoulder from gamma-rays is particularly problematic. The 2.6 MeV gamma-ray from  $^{208}\text{Tl}$  decay is the highest energy gamma from these decay chains and therefore isotopes above 2.6 MeV are preferred. Experiments using isotopes with Q-values below this energy must compensate with improved background rejection techniques.

Most of the high Q-value candidates[32] have been considered as a dopant for a liquid scintillator:  $^{150}\text{Nd}$  (Q=3.367 MeV)[33, 34],  $^{96}\text{Zr}$  (Q=3.350 MeV)[35],  $^{100}\text{Mo}$  (Q=3.034 MeV)[36],  $^{82}\text{Se}$  (Q=2.995 MeV)[37],  $^{116}\text{Cd}$  (Q=2.81 MeV)[37, 38],  $^{130}\text{Te}$  (Q=2.533 MeV)[37, 39],  $^{136}\text{Xe}$  (Q=2.479 MeV)[15] and  $^{124}\text{Sn}$  (Q=2.29 MeV)[40]. Xenon gas readily dissolves into liquid scintillator. For the other isotopes, a suitable organometallic compound needs to be found that produces a stable scintillator with a long attenuation length in the wavelength region of interest. Recently nanocrystals formed by candidate isotopes have been explored as an alternative to doping by single atoms,[37, 41].

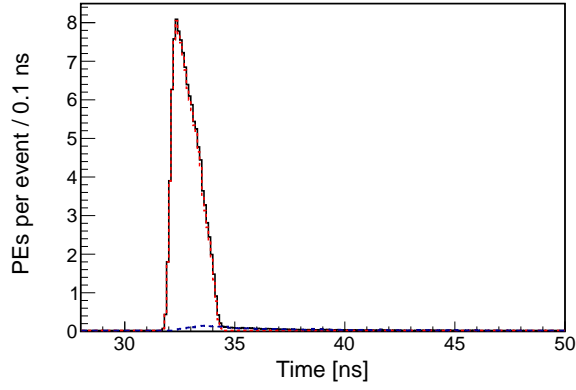


**Figure 2.** Photoelectron (PE) arrival times after application of the transit-time spread (TTS) for the simulation of 1000 electrons (5 MeV). The default simulation is shown with optical scattering turned on: all photons (black), un-scattered photons (red dotted), and scattered (blue dashed). Scattering causes a very small tail at longer times as expected.

### 3. Geant4 simulation

In order to study the effects relevant to directional reconstruction in liquid scintillators, a GEANT4 [42, 43] simulation has been constructed. The simulation uses GEANT4 version 4.9.6 with the default liquid scintillator optical model, in which optical photons are assigned the group velocity in the wavelength region of normal dispersion.

The detector geometry is a sphere of 6.5 m radius filled with scintillator. Figure 1 shows the geometry and the Cherenkov light from an example  $^{116}\text{Cd } 0\nu\beta\beta$  event. The default scintillator properties have been chosen to match a KamLAND-like scintillator[44]: 80% n-dodecane, 20% pseudocumene and 1.52 g/l PPO. The scintillator properties implemented in the simulation include the atomic composition and density ( $\rho = 0.78$  g/ml), the wavelength-dependent attenuation length[45] and refractive index[46], the scintillation emission spectrum[45], emission rise time ( $\tau_r = 1.0$  ns) and emission decay time constants ( $\tau_{d1} = 6.9$  ns and  $\tau_{d2} = 8.8$  ns with relative weights of 0.87 and 0.13)[47], scintillator light yield (9030 photons/MeV) and the Birks constant ( $kB \approx 0.1$  mm/MeV)[48]. This is a standard scintillator. The most critical value is the attenuation length at 400 nm which is 25 m. The attenuation length drops precipitously at 370 nm from 6.5 m to 0.65 m at the cutoff wavelength at 360 nm. Variations from the baseline KamLAND case are discussed below.

Re-emission of absorbed photons in the scintillator bulk volume and optical scattering, specifically Rayleigh scattering, have not yet been included by default. A test simulation shows that the effect of optical scattering is negligible. As shown in figure 2, scattering causes a small tail at longer times. The reason is that the cutoff is very steep below 360 nm and almost no photons reach the sphere, so optical scattering makes no difference for short wavelengths. Above about 395 nm, the attenuation length is greater than 20 m so both scattering and absorption are not very likely and scattering is negligible. The intermediate region is rather small. A similar argument holds for re-emission. Scattering length measurements and discussions can be found in Ref. [49].

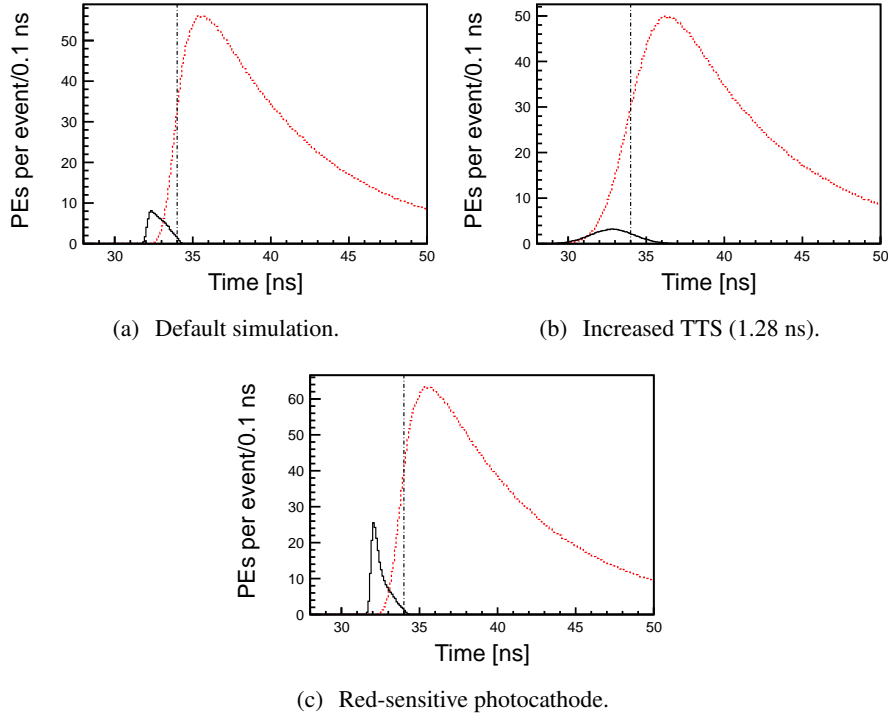


**Figure 3.** Photoelectron (PE) arrival times after application of the transit-time spread (TTS) for the simulation of 1000 electrons (5 MeV) with different values of the TTS and wavelength response. PEs from Cherenkov light (black, solid line) and scintillation light (red, dotted line) are compared. The dash-dotted vertical line illustrates a time cut at 34.0 ns. (a) Default simulation: bialkali photocathode and TTS = 0.1 ns ( $\sigma$ ). After the 34.0 ns time cut, 171 PEs from scintillation and 108 PEs from Cherenkov light are detected. (b) Default simulation settings except for TTS = 1.28 ns (KamLAND 17-inch PMTs). After the 34.0 ns time cut, 349 PEs from scintillation and 88 PEs from Cherenkov light are detected. (c) Default simulation settings except for a GaAsP photocathode. After the 34.0 ns time cut, 226 PEs from scintillation and 229 EPS from Cherenkov light are detected.

157 The inner sphere surface is used as the photodetector. It is treated as fully absorbing (no  
 158 reflections), with a photodetector coverage of 100%. As in the case of optical scattering, reflections  
 159 at the sphere are a small effect that would create a small tail at longer times. Two important  
 160 photodetector properties have been varied: 1) the transit-time spread (TTS, default  $\sigma = 0.1$  ns) and  
 161 2) the wavelength-dependent quantum efficiency (QE) for photoelectron production. The default is  
 162 the QE of a bialkali photocathode (Hamamatsu R7081 PMT)[50]. The QE values as a function of  
 163 wavelength come from the Double Chooz[4] Monte Carlo simulation. We note that the KamLAND  
 164 17-inch PMTs use the same photocathode type with similar quantum efficiency.

165 Four effects primarily contribute to the timing of the scintillator detector system: the travel  
 166 time of the particle, the time constants of the scintillation process, chromatic dispersion, and the  
 167 timing of the photodetector. First, the simulated travel time of a 5 MeV electron is  $0.108 \pm 0.015$  ns.  
 168 This corresponds to an average path length of 3.1 cm and a final distance from the origin of 2.6 cm.  
 169 The time until the electron drops below Cherenkov threshold is  $0.106 \pm 0.015$  ns. We note that due



to scattering the final direction of the electron before it stops does not correspond to the initial direction; however before the electron drops below Cherenkov threshold the scattering angle is small and therefore the Cherenkov light encodes the direction of the primary electron. The scattering physics is handled by Geant4's "Multiple Scattering" process which is valid down to 1 keV, where atomic shell structure becomes important[51]. In the energy range important for  $0\nu\beta\beta$ , a 1.4 MeV electron travels a total path length of 0.8 cm, has a distance from the origin of 0.6 cm in  $0.030\pm0.004$  ns and takes  $0.028\pm0.004$  ns to drop below Cherenkov threshold. The scattering follows the same pattern.

The scintillator-specific rise and decay times are the second effect that determines the timing in a scintillator detector. The first step in the scintillation process is the transfer of energy from the solvent to the solute. The time constant of this energy transfer accounts for a rise time in scintillation light emission. Past neutrino experiments were not highly sensitive to the effect of the scintillation rise time, which is the reason why there is a lack of accurate numbers. We assume a rise time of 1.0 ns; more detailed studies are needed in the future. The two time constants used to describe the falling edge of the scintillator emission time distribution (quoted above) are values specific to the KamLAND scintillator.

Chromatic dispersion is the third effect that determines the timing in a scintillator detector. Due to the wavelength-dependence of the refractive index the speed of light in the scintillator (see Equation (2.2)) increases with increasing photon wavelengths for normal dispersion, with red light traveling faster than blue light. In order to study the time differences due to this chromatic dispersion, we used a simplified simulation of 5 MeV electrons at the center of the sphere where we used instantaneous scintillation emission with the quantum-efficiency applied, but not including a transit-time spread. The higher energy 5 MeV electron provides larger photon statistics with which to evaluate the method, debug the simulation, and is of interest to neutrino-electron scattering experiments. The true hit time distributions of photoelectrons were analyzed for scintillation light and Cherenkov light separately. Photoelectrons coming from Cherenkov light are on average created about 0.5 ns earlier than PEs from scintillation light. The RMS values from PE time distributions for Cherenkov and scintillation light are both about 0.5 ns. Note that these numbers include the effect of the finite electron travel time.

The fourth effect determining the timing in a scintillator detector is the timing of the photodetectors. The measurement of the arrival times of single photoelectrons is affected by the transit-time spread (TTS) of the photodetectors, a number which can be different by orders of magnitude depending on the detector type. The default TTS of 0.1 ns ( $\sigma$ ) can be achieved with large area picosecond photodetectors (LAPPDs)[52–55] and possibly hybrid photodetectors (HPDs)[56]; even significantly lower TTS numbers are realistic with the LAPPD[53–55].

In sections 4 to 6, we study the photoelectron timing for different detector configurations at 5 MeV. We focus on the idea of increasing the discrimination between Cherenkov and scintillation light by using improved detector timing. The primary quantities provided by the GEANT4 simulation are the photoelectron hit positions and the detection times after the TTS resolution has been applied. In section 7 these quantities are then used for event reconstruction. With the successful reconstruction at 5 MeV, we then lower the energy of the simulated electrons and show that it is possible to reconstruct electrons in the range interesting for  $0\nu\beta\beta$ .



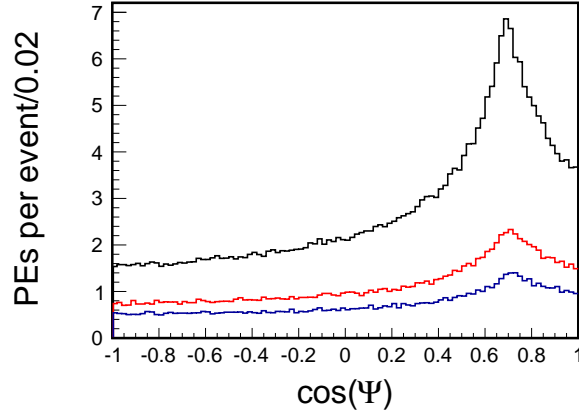


**Figure 4.** The angular distribution of photoelectron hits relative to the original electron direction,  $\cos(\Psi) = x_{hit}/|\vec{r}_{hit}|$ . Three energies are shown: 5 MeV (Black - Top), 2.1 MeV (Red - Middle), 1.4 MeV (Blue - Bottom). Each sample consists of 1000 events produced at the detector center. Default simulation settings are used and both Cherenkov and scintillation light are included. The  $t \leq 34.0$  ns cut is applied.

#### 4. Detector timing

We first discuss results for the default simulation settings described in the previous section. Figure 3 (a) shows the TTS-smeared photoelectron (PE) detection times for 1000 simulated electrons with 5 MeV energy in the center of the detector, with initial momentum directions coinciding with the x-axis. The photoelectrons induced by Cherenkov light arrive earlier, as expected due to the instantaneous emission and the higher average photon speed compared to scintillation light. There is, however, significant overlap of the two arrival time distributions.

In order to compare simulations with different parameters, a fixed time cut of  $t \leq 34.0$  ns is applied using the truth information to isolate the Cherenkov light in this early time window, as shown in figure 3 (a). For the default simulation case, the average number of PEs per event coming from Cherenkov light in the early time window (108) is 98% of the total average number of PEs from Cherenkov light (110). For scintillation light, the average number of PEs (171) is only 3.1% of the average total scintillation-induced PEs (5445). This demonstrates the effectiveness of a time cut to separate Cherenkov light from scintillation light.

The ratio of Cherenkov-induced to scintillation-induced photoelectrons in the early time window ( $R_{C/S}$ ) is a useful figure-of-merit when comparing different simulation settings, since a higher ratio means more directional information per PE. For the default simulation settings  $R_{C/S} = 0.63$ .

Figure 4 displays the angular distribution of PE hits after the time cut. Although this time cut is a simplification of actual time reconstruction effects, we can use it to indicate the spatial distribution of hits in the early time window. The Cherenkov ring structure can be clearly seen in the peak near  $46^\circ$ , demonstrating that the directional signal conveyed by the Cherenkov photons is not erased by scattering of the initial electrons even at 1.4 MeV.

When the 17-inch KamLAND PMTs[45, 57] (TTS = 1.28 ns) are used in the simulation, the broadening of the time distributions leads to a strongly decreased ratio of Cherenkov over scintillation light ( $R_{C/S} = 0.25$ ) for  $t < 34.0$  ns (see figure 3 (b)). This shows that a photodetector with

a low TTS is critical for directionality reconstruction and motivates the use of novel photodetector types.

## 5. Detector wavelength response

Since Cherenkov photons that pass through meters of scintillator have on average longer wavelengths than scintillation photons, a photodetector that is more sensitive at long wavelengths increases not only the absolute number of PEs but also the ratio between Cherenkov- and scintillation-induced PEs. We have run the simulation with the QE of an extended red-sensitive GaAsP photocathode (Hamamatsu R3809U-63)[58], but with the default TTS of 0.1 ns. Figure 3(c) shows the results for the modified simulation with high QE in the red spectral region. The higher absolute number of photoelectrons coming from Cherenkov light (factor of  $\approx 2$ ) and the increased Cherenkov/scintillation ratio ( $R_{C/S} = 1.01$ ) in the early time window would significantly improve the directionality reconstruction.

## 6. Scintillator emission spectrum

An alternative route towards increasing the separation in time between Cherenkov and scintillation photon hits is the tuning of the scintillator emission spectrum. Recently, the use of quantum dots (QDs) in liquid scintillators has been studied as a possibility to improve future large scale neutrino experiments[37, 41]. One major motivation for quantum-dot-doped scintillator is control of the emission spectrum by tuning the size or composition of the quantum dots.

Quantum dots can also provide a mechanism for introducing an isotope for studying double-beta decay. The emission spectrum of commercial alloyed core/shell  $\text{CdS}_x\text{Se}_{1-x}/\text{ZnS}$  quantum dots was measured in Ref.[41]. This spectrum shows a symmetric peak centered around 461 nm with  $\text{FWHM} = 29$  nm. In order to isolate the effect of the different emission spectrum, the other simulation settings, including the KamLAND absorption spectrum, were kept unchanged; we find  $R_{C/S} = 0.17$  for the default 34.0 ns timing cut. Compared to the default case shown in figure 3(a), the separation is worse (as expected) because the scintillation light wavelengths are longer than in the KamLAND emission spectrum.

However, advances in the production of commercial quantum dot samples could yield quantum dots which have similar, single peak emission shapes at shorter wavelengths. This case has been simulated using the same spectral shape of the measured core-shell quantum dot emission but shifted to shorter wavelengths such that the emission peak is centered at 384 nm. This peak emission value has been measured for other types of QDs, however with a much more pronounced tail[41]. The resulting PE time distribution shows improved separation of Cherenkov and scintillation light compared to the default simulation. After the 34.0 ns cut on the TTS-smeared PE time we obtain a Cherenkov/scintillation ratio of  $R_{C/S} = 0.86$  (107 PE from Cherenkov light and 124 PE from scintillation). The number of Cherenkov-induced PEs after the time cut is unchanged while the number of PEs coming from scintillation light is decreased due to the higher average photon travel times.

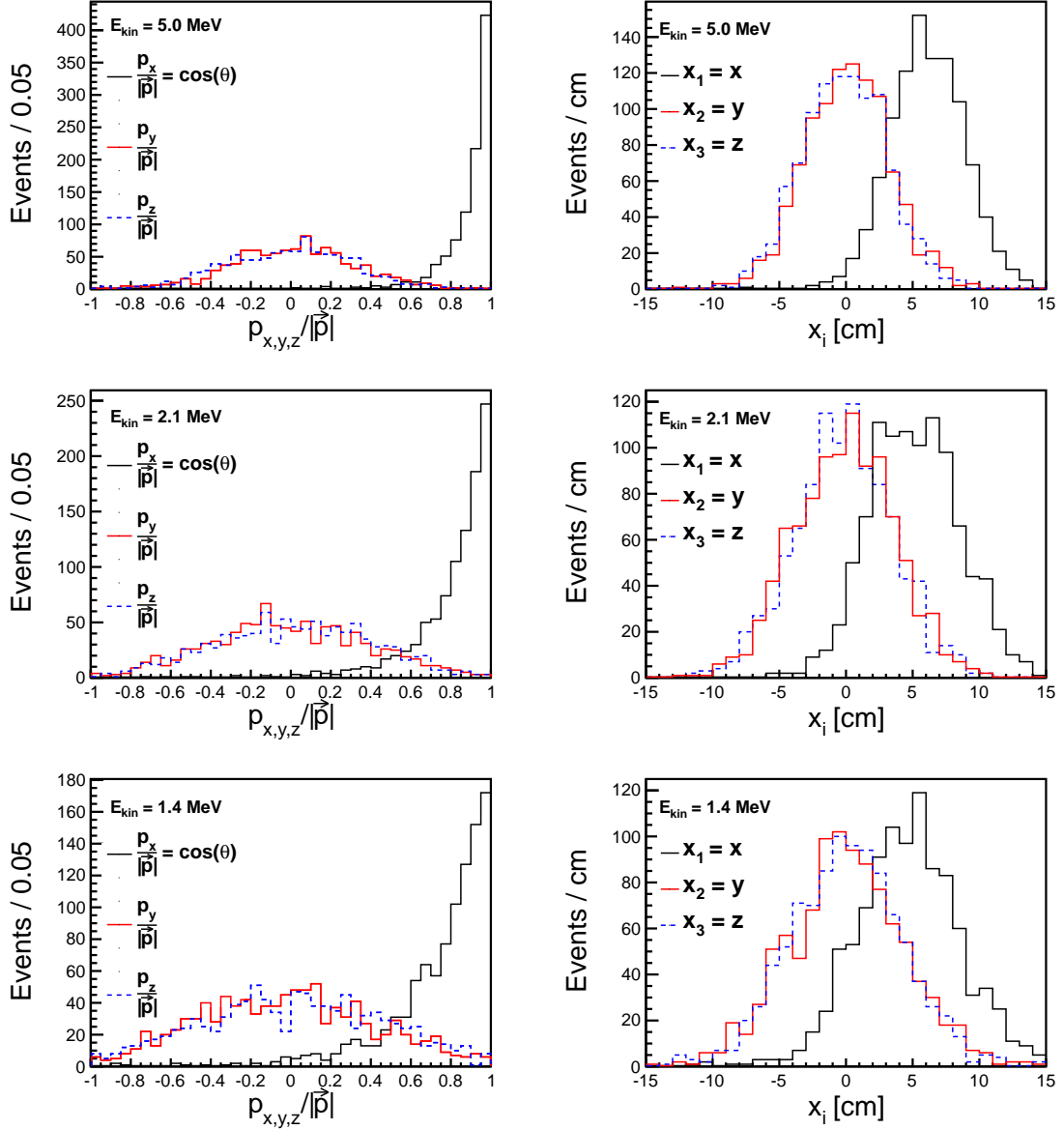


**Figure 5.** (Left) The reconstructed direction,  $(p_x/|\vec{p}|, p_y/|\vec{p}|, p_z/|\vec{p}|)$ , for the simulation of 1000 electrons. In the simulation the electrons are produced along the x-axis,  $\vec{p}/|\vec{p}| = (1,0,0)$ , and originate from the center of the 6.5m-radius detector,  $\vec{r} = (0,0,0)$ . Only photons with arrival time of  $t < 34.0$  ns are used in the reconstruction. The quantum efficiency of the bialkali photocathode is taken into account. (Right) The reconstructed vertex position,  $(x,y,z)$ , for the same simulation. From Top to Bottom, 5 MeV, 2.1 MeV and 1.4 MeV are shown.

## 274 7. Reconstruction

275 The timing studies show that in the early time window,  $t \leq 34.0$  ns, the ratio  $R_{C/S}$  is high, im-  
 276 proving the photoelectron hit selection. In this section, we apply reconstruction tools for a water  
 277 Cherenkov detector, WCSimAnalysis, to the problem of reconstructing the position and direction

of 5 MeV electrons from this early light. WCSimAnalysis is a water Cherenkov reconstruction package developed by the Long Baseline Neutrino Experiment (LBNE) Collaboration[59]. It provides a framework for generic event cleaning, track reconstruction, and particle identification, and comes equipped with variety of pre-built algorithms. It is continuing to be expanded using new track-fitting techniques for water Cherenkov detectors[60] based on advanced photosensors with sub-cm imaging capabilities and timing resolutions below 100 picoseconds.

To start, we are neglecting the effects of position dependence. In future work the arrival times can be corrected by the time of flight from the reconstructed vertex and the position and direction fitted simultaneously. For isotropic light, the vertex reconstruction uncertainty leads to an additional smearing of the arrival time distribution of 0.15 ns for every 3 cm of position reconstruction uncertainty. For directional light, the vertex reconstruction uncertainty leads to an effective shift of the arrival time distribution. This would change the ideal time cut by 0.15 ns for every 3 cm of position reconstruction uncertainty. We have studied other time cuts from 33 ns to 34.5 ns and the reconstruction remained reasonable.

The results presented in this paper rely on a simple vertex reconstruction algorithm, commonly known as a “point fit”[61]. It assumes that all of the scintillation and Cherenkov light is emitted from a single point in space-time  $(x_0, y_0, z_0, t_0)$ . In actuality, the light is emitted along a multi-scattered electron track. However, at the energies discussed in this paper, the extent of this track is small (a few cm) compared to the scale of the detector ( $R=6.5$  meters) that sets the typical photon transit distances.

The first step of the reconstruction process relies on exact numerical calculations of vertex candidates from quadruplets of hits. Given a single point source, we need four constraints to solve for the four unknowns of the vertex  $(x, y, z, t_0)$ [62]. This approach would provide an exact solution in the case of four prompt, un-scattered photons originating from a common point. However, many of these randomly chosen quadruplets will produce anomalous solutions due to ‘real world’ effects such as delayed emission and deviations from the point-like geometry. Nonetheless, we found that any chosen subset of 400 quadruplets was a sufficiently large ensemble to assure that some solutions will be close to the true vertex.

Once a set of vertex candidates has been found, we test the goodness of each vertex and select the one that best fits the full ensemble of photon hits. The goodness of fit is determined based on the distribution of an observable known as the “point time residual”[61]. The point time residual is calculated by first choosing a hypothesis for the vertex position and  $t_0$  for the event. The goodness of fit for these values is then calculated by taking the difference between the measured and predicted times of each photon hit, using a single effective speed of light in the scintillator. The width of the time residual distribution over all hits is minimized when the hypothesized vertex is near the true vertex. Based on this figure of merit, we select the vertex with the narrowest time residual distribution from among the 400 candidates.

The direction of the electron track is then determined by taking the centroid of all vectors pointing from the fitted vertex to the hits on the detector. Since the Cherenkov light is highly directional, and since the timing cut enhances the purity of the Cherenkov light in the sample, this calculation provides a good measure of the track direction.

For the purpose of testing the reconstruction algorithm we use 1000 simulated electrons with an energy of 5 MeV; lower energies are studied in the next section. The electrons are simulated at

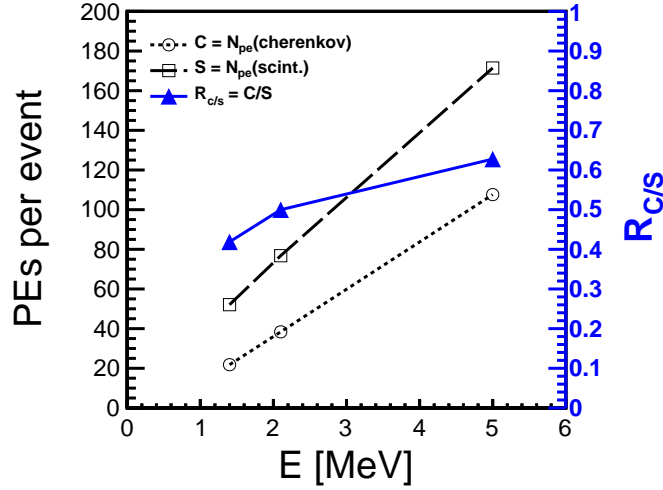


**Figure 6.** The energy dependence of the mean number of PEs after the 34.0 ns time cut is shown for Cherenkov-induced PEs (black open circles, dotted line) and scintillation-induced PEs (black open squares, dashed line). The ratio between the mean number of Cherenkov-induced and scintillation-induced PEs is shown as blue filled triangles, values are given on the right y-axis. The statistical errors are too small to be seen.

the center of the detector,  $\vec{r} = (0,0,0)$ , along the x-axis,  $\vec{p}/|\vec{p}| = (1,0,0)$ . Figure 5 (Top) shows the vertex reconstruction. The vertex is reasonably well-reconstructed around the center of the detector,  $\vec{r} = (0,0,0)$ , except along the x-axis. The RMS values of the distributions for all three reconstructed coordinates are smaller than 3.5 cm. The shift along the x-axis is due to two effects for which the reconstruction has to use average values rather than the unknown true value for each hit: the wavelength and hence the speed of the light in the medium, and the point of emission for each of the photons, reconstructed as coming from a common point. The reconstruction of the direction also is shown in figure 5 (Top). It shows that for the majority of the events the initial electron direction is reconstructed well. This is a promising result given the simplicity of the algorithms used.

## 8. Energy dependence

In the previous sections we presented results on single 5 MeV electrons such as might be observed in neutrino-electron scattering. In this section we study two lower energies, 1.4 MeV and 2.1 MeV, appropriate for searches for  $0\nu\beta\beta$ . These energies correspond to  $Q/2$  for the double-beta decay of  $^{116}\text{Cd}$  and  $^{48}\text{Ca}$ , respectively[38, 39]. The isotope  $^{116}\text{Cd}$  was chosen because of its potential use in quantum-dot-doped scintillators[37, 41] and  $^{48}\text{Ca}$  was chosen to cover the  $Q$ -value range of  $0\nu\beta\beta$  candidate isotopes.

The two additional simulation sets with 1.4 MeV and 2.1 MeV electrons were generated using the default simulation configuration described in section 3. The PE time distribution for the default settings is shown in figure 3 (a) for 5 MeV electrons. The shapes of the scintillation and Cherenkov spectra are similar for the lower energies (not shown here). In figure 6, the energy-dependent

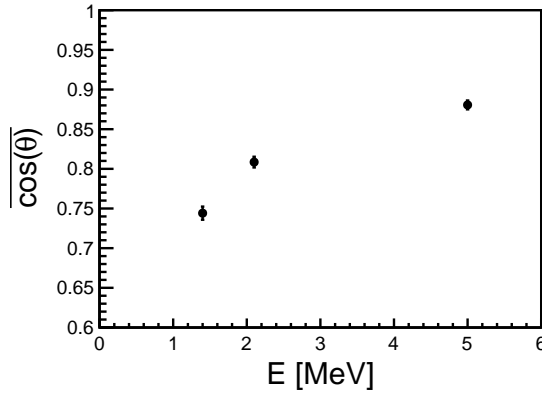


**Figure 7.** Mean cosine of the angle between the true initial electron direction and the reconstructed direction, as a function of the electron energy. For each energy 1000 events have been simulated. Statistical errors are shown.

mean number of PEs per event after the 34.0 ns time cut is shown for Cherenkov-induced and scintillation-induced PEs, as well as their ratio  $R_{C/S}$ . The mean number of PEs from Cherenkov (scintillation) light for electron energies 1.4(2.1) MeV is 21.8 (52.1), 38.4 (76.8) and 108 (171) for 1.4 MeV, 2.1 MeV and 5 MeV, respectively. This gives the ratios  $R_{C/S} = 0.42, 0.50$  and  $0.63$ : The decrease in Cherenkov-induced PEs is stronger than the decrease in scintillation-induced PEs as the energy is lowered.

The reconstruction algorithms outlined in section 7 have also been applied to the simulations at lower energies. Figure 5 (Middle) shows the results for 2.1 MeV and figure 5 (Bottom) shows the results for 1.4 MeV. Most events are still reconstructed well, despite the lower number of PEs and the decreased  $R_{C/S}$ . For 1.4 MeV electrons, the RMS values of the distributions for all three reconstructed coordinates are smaller than 4.5 cm. The mean cosine of the angle between the true direction and the reconstructed direction for different energies of the initial electron is shown in figure 7. The direction reconstruction performance is still promising for energies as low as 1.4 MeV.

## 9. Conclusions

We developed a technique to separate scintillation and Cherenkov light to reconstruct direction of electrons with energies 5 MeV, 2.1 MeV and 1.4 MeV in a liquid scintillator detector. These energies were chosen to represent typical neutrino-electron elastic scattering energies and  $0\nu\beta\beta$  energies. The Cherenkov threshold for an electron in a typical liquid scintillator is  $\sim 0.2$  MeV

While scintillation light is isotropic, Cherenkov light with wavelengths above  $\sim 370$  nm carries the information about the direction of the electrons. All light shorter than  $\sim 370$  nm get absorbed and re-emitted isotropically as a part of the scintillation process. On average scintillation light is delayed with respect to the direct Cherenkov light due to chromatic dispersion and the finite rise time of the scintillation. Therefore early light contains directional information.

Using a GEANT simulation of a spherical detector with radius of 6.5 m, we showed that for electrons originated at the center, Cherenkov light arrives on average  $\sim 1$  ns before the scintillation light. Chromatic dispersion alone accounts for  $\sim 0.5$  ns delay between scintillation and Cherenkov light. We then defined an early time window and found for a 5 MeV electron that the ratio of Cherenkov to scintillation light is 0.63 for photodetectors with TTS of 0.1 ns. This was degraded by a factor of 2.5 if current photodetectors with  $\sim 1$  ns resolution were used. This can be improved by 1.6 or 1.4 if more red sensitive photodetectors or scintillators with narrower emission spectra are used

We applied reconstruction algorithms from water Cherenkov detectors. QUANTATIVE STATEMENT ABOUT VERTEX DIRECTION PERFORMANCE.

We find the technique promising and plan to continue work on the topic. The ability to reconstruct direction in kiloton-scale scintillation detectors would expand capabilities of neutrino experiments, especially those also searching for neutrino-less double-beta decay. More generally, this technique could be applied wherever scintillation-based detectors are used.

## Acknowledgments

The authors thank Andrew Blake at University of Cambridge for his work authoring the WCSimAnalysis code. The authors thank the neutrino reconstruction group at Iowa State, particularly Mayly Sanchez, Ioana Anghel, and Tian Xin, for their continued work in developing the WCSimAnalysis algorithms and for their insights and expertise regarding issues related to Cherenkov reconstruction with fast-timing. The authors also thank Michael Smy for his development of the quadruplet-based vertex-finding method. L. Winslow would like to thank Janet Conrad for many useful discussions on the topic, and Katsushi Arisaka for discussions on the possible reach of traditional PMTs and the characteristics of HPDs. C. Aberle and L. Winslow are supported by funds from University of California Los Angeles. The work at the University of Chicago is partially supported by DOE contract DE-SC0008172 and NSF grant PHY-1066014. Matthew Wetstein gratefully acknowledges support by the Grainger Foundation.



## References

- [1] **KamLAND** Collaboration, A. Gando et al., *Reactor On-Off Antineutrino Measurement with KamLAND*, arXiv:1303.4667.
- [2] **Borexino** Collaboration, G. Bellini et al., *Precision measurement of the  $^7\text{Be}$  solar neutrino interaction rate in Borexino*, *Phys. Rev. Lett.* **107** (2011) 141302, [arXiv:1104.1816].
- [3] **Daya Bay** Collaboration, F. An et al., *Improved Measurement of Electron Antineutrino Disappearance at Daya Bay*, *Chin. Phys.* **C37** (2013) 011001, [arXiv:1210.6327].
- [4] **Double Chooz** Collaboration, Y. Abe et al., *Reactor electron antineutrino disappearance in the Double Chooz experiment*, *Phys. Rev.* **D86** (2012) 052008, [arXiv:1207.6632].
- [5] **Double Chooz** Collaboration, Y. Abe et al., *First Measurement of  $\theta_{13}$  from Delayed Neutron Capture on Hydrogen in the Double Chooz Experiment*, *Phys. Lett.* **B723** (2013) 66, [arXiv:1301.2948].
- [6] **RENO** Collaboration, J. K. Ahn et al., *Observation of Reactor Electron Antineutrinos Disappearance in the RENO Experiment*, *Phys. Rev. Lett.* **108** (2012) 191802.
- [7] Y.-F. Li, J. Cao, Y. Wang, and L. Zhan, *Unambiguous Determination of the Neutrino Mass Hierarchy Using Reactor Neutrinos*, arXiv:1303.6733.
- [8] *RENO-50 - International Workshop on toward Neutrino Mass Hierarchy*, June, 2009.
- [9] J. Conrad, M. Shaevitz, I. Shimizu, J. Spitz, M. Toups, and L. Winslow, *Precision  $\bar{\nu}_e$ -electron Scattering Measurements with IsoDAR to Search for New Physics*, arXiv:1307.5081. In preparation, for submission to *Phys. Rev. D*.
- [10] **IsoDAR** Collaboration, A. Bungau et al., *Proposal for an Electron Antineutrino Disappearance Search Using High-Rate  $^8\text{Li}$  Production and Decay*, *Phys. Rev. Lett.* **109** (2012) 141802, [arXiv:1205.4419].
- [11] K. Heeger, B. Littlejohn, and H. Mumm, *Multiple Detectors for a Short-Baseline Neutrino Oscillation Search Near Reactors*, arXiv:1307.2859.
- [12] A. Porta et al., *Reactor Neutrino Detection for Non-Proliferation With the NUCIFER Experiment*, *Nuclear Science, IEEE Transactions on* **57** (2010) 2732–2739.
- [13] N. Bowden et al., *Experimental results from an antineutrino detector for cooperative monitoring of nuclear reactors*, *Nucl. Instrum. Meth.* **A572** (2007) 985 – 998.
- [14] M. Fukugita and T. Yanagida, *Barygenesis without grand unification*, *Physics Letters B* **174** (1986), no. 1 45 – 47.
- [15] **KamLAND-Zen** Collaboration, A. Gando et al., *Limit on Neutrinoless  $\beta\beta$  Decay of Xe-136 from the First Phase of KamLAND-Zen and Comparison with the Positive Claim in Ge-76*, *Phys. Rev. Lett.* **110** (2013) 062502, [arXiv:1211.3863].
- [16] **GERDA** Collaboration, M. Agostini et al., *Results on neutrinoless double beta decay of  $^{76}\text{Ge}$  from GERDA Phase I*, *Phys.Rev.Lett.* **111** (2013) 122503, [arXiv:1307.4720].
- [17] **CUORE** Collaboration, F. Alessandria et al., *Sensitivity of CUORE to Neutrinoless Double-Beta Decay*, arXiv:1109.0494.
- [18] **SuperNEMO Collaboration** Collaboration, R. Arnold et al., *Probing New Physics Models of Neutrinoless Double Beta Decay with SuperNEMO*, *Eur.Phys.J.* **C70** (2010) 927–943, [arXiv:1005.1241].

- [19] **EXO** Collaboration, M. Auger et al., *Search for Neutrinoless Double-Beta Decay in  $^{136}\text{Xe}$  with EXO-200*, *Phys. Rev. Lett.* **109** (Jul, 2012) 032505.
- [20] **NEXT** Collaboration, V. Alvarez et al., *Operation and first results of the NEXT-DEMO prototype using a silicon photomultiplier tracking array*, *JINST* **8** (2013) P09011, [arXiv:1306.0471].
- [21] J. G. Learned, *High Energy Neutrino Physics with Liquid Scintillation Detectors*, arXiv:0902.4009.
- [22] R. Luscher et al., *Search for beta beta decay in Xe-136: New results from the Gotthard experiment*, *Phys.Lett.* **B434** (1998) 407–414.
- [23] A. Ali, A. Borisov, and D. Zhuridov, *Probing new physics in the neutrinoless double beta decay using electron angular correlation*, *Phys.Rev.* **D76** (2007) 093009, [arXiv:0706.4165].
- [24] **CHOOZ** Collaboration, M. Apollonio et al., *Search for neutrino oscillations on a long baseline at the CHOOZ nuclear power station*, *Eur.Phys.J.* **C27** (2003) 331–374, [hep-ex/0301017].
- [25] K. A. Hochmuth, M. Lindner, and G. G. Raffelt, *Exploiting the directional sensitivity of the Double Chooz near detector*, *Phys.Rev.* **D76** (2007) 073001, [arXiv:0704.3000].
- [26] J.B. Birks, *The Theory and Practice of Scintillation Counting*. Pergamon Press, 1964.
- [27] P. A. Cherenkov, *Visible emission of clean liquids by action of gamma radiation*, *Doklady Akademii Nauk SSSR* **2** (1934) 451.
- [28] A. M. Steinberg, P. G. Kwiat, and R. Y. Chiao, *Dispersion cancellation in a measurement of the single-photon propagation velocity in glass*, *Phys. Rev. Lett.* **68** (1992) 2421–2424.
- [29] **Particle Data Group** Collaboration, J. Beringer et al., *Review of Particle Physics (RPP)*, *Phys. Rev.* **D86** (2012) 010001.
- [30] I. Tamm, *Radiation Emitted by Uniformly Moving Electrons*, *J. Phys. U.S.S.R.* **1** (1939) 439.
- [31] F. Boehm and P. Vogel, *Physics of Massive Neutrinos*. Cambridge University Press, 1992.
- [32] V. Tretyak and Y. Zdesenko, *Tables of double beta decay data*, *Atomic Data and Nuclear Data Tables* **61** (1995) 43 – 90.
- [33] M. Yeh, Y. Williamson, and R. L. Hahn, *Metal-loaded liquid scintillators for neutrino experiments*, *J. Phys. Conf. Ser.* **136** (2008) 042054.
- [34] I. Barabanov et al., *A Nd-loaded liquid organic scintillator for the experiment aimed at measuring double beta decay*, *Instrum. Exp. Tech.* **55** (2012) 545–550.
- [35] Y. Fukuda, S. Moriyama, and I. Ogawa, “Development of liquid scintillator containing a zirconium complex for neutrinoless double beta decay experiment.” article in press, *Nucl. Instrum. Meth. A*, 2013.
- [36] V. Gehman, P. Doe, R. Robertson, D. Will, H. Ejiri, and R. Hazama, *Solubility, Light Output and Energy Resolution Studies of Molybdenum-Loaded Liquid Scintillators*, *Nucl. Instrum. Meth.* **A622** (2010) 602–607, [arXiv:0911.2198].
- [37] L. Winslow and R. Simpson, *Characterizing quantum-dot-doped liquid scintillator for applications to neutrino detectors*, *Journal of Instrumentation* **7** (2012) P07010.
- [38] G. Bellini et al., *High sensitivity 2 beta decay study of Cd-116 and Mo-100 with the BOREXINO counting test facility (CAMEO project)*, *Eur. Phys. J.* **C19** (2001) 43–55, [nucl-ex/0007012].

- [39] S. D. Biller, *Probing Majorana neutrinos in the regime of the normal mass hierarchy*, *Phys. Rev.* **D87** (2013) 071301, [arXiv:1306.5654].
- [40] **KIMS** Collaboration, M. Hwang et al., *Development of tin-loaded liquid scintillator for the double beta decay experiment*, *Nucl. Instrum. Meth.* **A570** (2007) 454–458.
- [41] C. Aberle, J. Li, S. Weiss, and L. Winslow, *Optical properties of quantum-dot-doped liquid scintillators*, *Journal of Instrumentation* **8** (2013) P10015, [arXiv:1307.4742].
- [42] **GEANT4** Collaboration, S. Agostinelli et al., *GEANT4: A Simulation toolkit*, *Nucl. Instrum. Meth.* **A506** (2003) 250–303.
- [43] J. Allison et al., *Geant4 developments and applications*, *Nuclear Science, IEEE Transactions on* **53** (2006) 270–278.
- [44] **KamLAND** Collaboration, K. Eguchi et al., *First results from KamLAND: Evidence for reactor anti-neutrino disappearance*, *Phys. Rev. Lett.* **90** (2003) 021802, [hep-ex/0212021].
- [45] O. Tajima, *Development of Liquid Scintillator for a Large Size Neutrino Detector*, Master’s thesis, Tohoku University, 2000.
- [46] O. Perevozchikov, *Search for electron antineutrinos from the sun with KamLAND detector*. PhD thesis, University of Tennessee, 2009.
- [47] O. Tajima, *Measurement of Electron Anti-Neutrino Oscillation Parameters with a Large Volume Liquid Scintillator Detector, KamLAND*. PhD thesis, Tohoku University, 2003.
- [48] C. Grant, *A Monte Carlo Approach to  $^7\text{Be}$  Solar Neutrino Analysis with KamLAND*. PhD thesis, University of Alabama, 2012.
- [49] M. Wurm, F. von Feilitzsch, M. Goeger-Neff, M. Hofmann, T. Lachenmaier, et al., *Optical Scattering Lengths in Large Liquid-Scintillator Neutrino Detectors*, *Rev.Sci.Instrum.* **81** (2010) 053301, [arXiv:1004.0811].
- [50] *Hamamatsu Photonics K.K., Large Photocathode Area Photomultiplier Tubes (data sheet, including R7081)*, accessed July, 2013. [http://www.hamamatsu.com/resources/pdf/etd/LARGE\\_AREA\\_PMT\\_TPMH1286E05.pdf](http://www.hamamatsu.com/resources/pdf/etd/LARGE_AREA_PMT_TPMH1286E05.pdf).
- [51] *Electromagnetic Standard Physics Working Group*, accessed December, 2013. [http://www.geant4.org/geant4/collaboration/working\\_groups/electromagnetic/index.shtml](http://www.geant4.org/geant4/collaboration/working_groups/electromagnetic/index.shtml).
- [52] B. Adams et al., *Measurements of the gain, time resolution, and spatial resolution of a  $20\times 20\text{cm}^2$  MCP-based picosecond photo-detector*, *Nucl.Instrum.Meth.* **A732** (2013) 392–396.
- [53] B. Adams et al., *Invited article: A test-facility for large-area microchannel plate detector assemblies using a pulsed sub-picosecond laser*, *Review of Scientific Instruments* **84** (2013) 061301.
- [54] E. Oberla, J. Genat, H. Grabas, H. Frisch, K. Nishimura, and G. Varner, “A 15 GSa/s, 1.5 GHz Bandwidth Waveform Digitizing ASIC.” submitted to *Nucl. Instrum. Meth. A*, 2013.
- [55] H. Grabas, R. Obaid, E. Oberla, H. Frisch, J.-F. Genat, R. Northrop, F. Tang, D. McGinnis, B. Adams, and M. Wetstein, *{RF} strip-line anodes for psec large-area mcp-based photodetectors*, *Nucl.Instrum.Meth. A* **711** (2013) 124 – 131.
- [56] Y. Kawai, *Development of a Hybrid Photon-Detector Module for Next Generation Water-Cherenkov Detectors*. PhD thesis, The Graduate University for Advanced Studies (SOKENDAI), 2007.
- [57] H. Kume et al., *20 INCH DIAMETER PHOTOMULTIPLIER*, *Nucl. Instrum. Meth.* **205** (1983) 443–449.

- 512 [58] *Hamamatsu Photonics K.K., R3809U-61/-63/-64 data sheet*, accessed July, 2013.  
513 [http://www.hamamatsu.com/resources/pdf/etd/R3809U-61-63-64\\_TPMH1295E04.pdf](http://www.hamamatsu.com/resources/pdf/etd/R3809U-61-63-64_TPMH1295E04.pdf).
- 514 [59] A. Blake, *WCSimAnalysis Reconstruction Package*. Cavendish Laboratory, University of  
515 Cambridge, UK.
- 516 [60] M. Sanchez and M. Wetstein, *Using Large Area Microchannel Plate Photodetectors in the Next*  
517 *Generation Water Cherenkov Neutrino Detectors*, *Nuclear Physics B - Proceedings Supplements*  
518 **229232** (2012) 525. Neutrino 2010.
- 519 [61] M. Ishitsuka, *L/E Analysis of the Atmospheric Neutrino Data From Super-Kamiokande*. PhD thesis,  
520 University of Tokyo, 2004.
- 521 [62] M. Smy for the Super-Kamiokande Collaboration, *Low Energy Event Reconstruction and Selection in*  
522 *Super-Kamiokande-III*, in *Proceedings of the 30th International Cosmic Ray Conference*  
523 (R. Caballero, J.C. D’Olivo, G. Medina-Tanco, L. Nellen, F.A. Sánchez, J.F. Valdés-Galicia, ed.),  
524 vol. 5, pp. 1279–1282, 2008.